# Strategic Astrophysics Technology

Milestone #2 Final Report

## *Linear Wavefront Control*

Dec 18, 2024

Olivier Guyon, P.I.
Phillip K Poon

Kyohoon Ahn, Julien Lozi, Jared Males, Matthew Noyes, Axel Potier, Camilo Mejia Prada, A J Eldorado Riggs, Garreth Ruane, Alex Walter

# Signature Page

E-SIGNED by Olivier Guyon
on 2024-12-19 05:09:11 GMT

Olivier Guyon, Principal Investigator Date

E-SIGNED by Nicholas Siegler
on 2024-12-19 00:16:53 GMT

Nick Siegler (ExEp Program Chief Technologist) Date
Exoplanet Exploration Program, NASA / JPL - California Institute of Technology

E-SIGNED by Brendan Crill
on 2024-12-18 22:57:36 GMT

Brendan Crill (Deputy ExEp Program Chief Technologist) Date
Exoplanet Exploration Program, NASA / JPL - California Institute of Technology

E-SIGNED by Lucas Paganini
on 2024-12-19 15:39:07 GMT

Lucas Paganini Date
ExEp Executive, NASA-HQ

# Executive Summary

The milestone completion described in this document is part of the NASA-funded effort “Linear Wavefront Control for High Contrast Imaging”, which is aimed at improving the efficiency, sensitivity, and reliability of wavefront control for exoplanet imaging.

As discussed in the previous completion report for Milestone 1, imaging planets in reflected light, a key focus of future NASA missions, requires advanced wavefront control to maintain a deep, temporally correlated null of stellar halo, called a dark hole (DH). Spectral Linear Dark Field Control (LDFC) is a wavefront stabilization technique, the spectral version of spatial LDFC. It uses bright starlight outside the science band to stabilize a deep null in a coronagraphic science band image. Spectral LDFC uses the response to perturbations in uncorrected, 'bright field' regions in the sensing band(s), to maintain a dark hole without continuous DM probing.

Results presented in this document are aimed at completing LDFC milestone #2 (MS2) defined in the LDFC Milestone #2 and Milestone #3 white paper:

**“Demonstrate a 10x suppression of injected disturbances by use of spectral LDFC stabilization in a dark hole with area covering at least 10 sq-lambda/D and reaching a raw contrast (post-LDFC) level below 1e-7.”**

We exceeded this milestone using NASA’s High Contrast Imaging Testbed (HCIT) facility Decadal Survey Testbed 2 (DST2), which conducted the first experimental demonstration of Spectral LDFC and the first demonstration of spatial or spectral LDFC at less than 1E-8 raw contrast. These tests were carried out at starting raw contrasts ranging from 1.8 to 6.8E-9 mean Normalized Intensity (NI) at angular separations of 3.5 to 8 λ/D in the science band scoring region.

In over 60 experiments, we corrected injected disturbances in the dark hole (DH) with a scoring region area greater than 10 squared $\lambda_{sci}$/D by a factor of 10 or more. The largest improvement factor was approximately 170. The correction was stable for over 100 iterations. In addition to previous results using spatial LDFC, these experimental results demonstrate spatial and spectral LDFC are promising alternatives to DM probing in low-flux regimes (which require at least two DM probes per control iteration and significantly longer integration time per control iteration).

Injected disturbances consisted of linear combinations of DM sine waves (did not include cosines), not representative of expected on-orbit wavefront disturbances.

# SAT Description

## Background and Motivation

Direct imaging of Earth-like exoplanets (exoEarths) orbiting stars similar to our Sun is difficult, primarily because the light these planets reflect is about 10 billion times dimmer than that of their parent stars (Traub et al 2010). A coronagraph must employ a wavefront sensing and control (WFSC) loop to correct for wavefront aberrations in order to establish regions of high contrast in the science image called dark

holes (DH). In this scenario, the WFSC algorithm must be able to sense and correct for wavefront errors at the picometer level (Crill 2022).

A typical example of WFSC for coronagraphs is the combination of pairwise probing (PWP) (Give'on et al 2011) and electric field conjugation (EFC) (Give'on et al 2007). Pairwise probing places known shapes on the deformable mirror (DM) which modulates the science camera image. By applying pairs of positive and negative probes, the difference image can be used to estimate the unknown electric field (Give'on et al 2007, Potier et al 2020). The estimate from PWP is the input of the EFC algorithm which then outputs a correction command to the deformable mirrors (Give'on et al 2009). This process, called "digging the dark hole"', is executed iteratively until the desired contrast is reached.

In practice, the telescope may need to point at a bright reference star to obtain the suitable SNR required to establish the DH contrast in a reasonable amount of time (Roman Space Telescope at IPAC 2022). Once the desired contrast level is achieved, the DM command is stored, and the telescope can then point at the fainter science target star. Due to the low flux of these exoplanets, the science exposure may take up to several days or longer. This requires the entire optical system to be extremely stable. In reality, slow changes to the wavefront, called quasi-static aberrations, will corrupt the contrast in the DH, requiring time and resources to point to another suitably bright star to re-establish the desired contrast. If the coronagraph can maintain the DH contrast without the need to point to a bright star, this capability will significantly improve science yield, reduce required observing time, and lower costs (Pogorelyuk et al 2022). Even in situations where the target star is bright enough, the use of traditional PWP interrupts the science acquisitions.

Another advantage of DH maintenance techniques is the potential to relax wavefront stability requirements on the hardware required for ultrastable space-based optical observatories (Crill 2022). Developing such hardware will be time consuming and expensive. An algorithmic approach which can utilize current hardware technologies would significantly reduce the cost of future direct imaging instruments.

A previously demonstrated set of methods employs an Extended Kalman Filter (EKF) that utilizes DM dithering for wavefront sensing (WFS) (Pogorelyuk et al 2019, Redmond et al 2020). This is followed by an EFC-based correction algorithm to sustain the DH. These methods depend on images captured at the science wavelength and need a number of these images to accurately determine the appropriate DM command for correcting quasi-static wavefront errors. Also, DM dithering compromises the DH's contrast, thereby interrupting the science exposure. The speed of the estimation algorithm is limited by the exposure time. Because these methods use the science wavelength, they require longer integration times to maintain deeper contrasts. Reducing the dither amplitude is possible but comes at the expense of estimator performance.

Developing a technique to maintain the DH contrast without interrupting the science acquisition is therefore desirable. Linear dark field control (LDFC) is a DH maintenance technique that does not require any modulation of the DM during the WFSC loop. In both varieties of LDFC, since the bright field has significantly more starlight than the DH, the changes in intensity are linear with small changes in wavefront error. The advantage of the linear relationship allows the use of linear control algorithms for WFSC to maintain the DH contrast. As discussed in prior work, LDFC is only intended as a DH maintenance procedure: it is not used to establish the initial DH.

**Spatial LDFC**, which was the first to be proposed (Miller et al 2017), senses changes in intensity in the spatial bright field to detect quasi-static wavefront errors; this has been experimentally demonstrated on

the Ames Coronagraph Experiment testbed (Currie et al 2020) and the Subaru Extreme Adaptive Optics testbed (Ahn et al, SPIE, 2022, Ahn et al, A&A, 2022). However, spatial LDFC can only be applied to stabilize the DH in a 180 degree field of view. **Spectral LDFC** is a related concept that uses the spectral bright field, which is the out-of-band light, called the sensing band, to perform wavefront sensing in the whole 360 degree field of view (Guyon et al 2017). Either a separate camera, a dual- or multi-band camera, or an integral field spectrometer (IFS) can be used to measure the intensity changes in the sensing band.

We can summarize LDFC's strengths and limitations below:

LDFC strengths

- **Sensitivity:** LDFC can use more light than available within the spatial and spectral extent of the dark hole, resulting in improved sensitivity.
- **DM probing-free:** Since no DM perturbations are required for the loop to operate, science acquisitions can be done at full duty cycle.
- **Ease of calibration:** As LDFC is a linear control technique, it uses differences of the pixel intensities relative to DM actuation for calibration. This calibration can be measured by DM probing in a reasonably short amount of time, so the technique is not as sensitive to modeling errors as EFC-like approaches that require a numerical model of the coronagraph system.
- **Linearity:** The linear control loop is fast to execute, and common high performance software for linear analysis techniques can be deployed for optimization and analysis.
- **Scalability:** Multiple sensors (cameras at multiple wavelengths) can easily be integrated in a LDFC control scheme, as no dark hole is required in the sensing bands and no DM probing is required.

LDFC limitations

- LDFC is a **differential** sensing technique that cannot by itself drive the system to a high contrast state.
- A **null space** may exist: not all wavefront modes can be sensed, and some of the unseen modes can negatively affect contrast.
- **Non-stationarity** of the relationship between bright field, wavefront state and dark hole illumination can build up over time.

Our NASA-funded SAT effort is aimed at validating both spatial and spectral LDFC. This document presents results for Milestone 2 (MS2), which was formulated in the MS#2 and MS#3 whitepaper, and focuses on spectral LDFC. Future demonstrations will also explore system-level LDFC operation in realistic conditions to improve the approach technology readiness level (TRL).

# Experimental Overview: Laboratory Setup

We conducted the demonstration of Spectral LDFC using the Decadal Survey Testbed 2 (DST2) (Noyes et al 2023), located at NASA's High Contrast Tested Facility (HCIT). The DST2 is housed inside a large vacuum chamber to simulate the pressure and thermal environment of a space-based coronagraph. The chamber can reach a pressure of less than 0.5 mTorr and exhibits thermal stability of $\sim 10$ mK. The optical system of DST2 is mounted on a carbon composite optical table, and the optical bench is mechanically isolated from the environment with three passive vibration isolators (MinusK CM-1). Both

passive and active thermal control are employed to reduce thermal expansion that would otherwise lead to quasi-static aberrations. The vacuum chamber itself is housed in a large cleanroom.

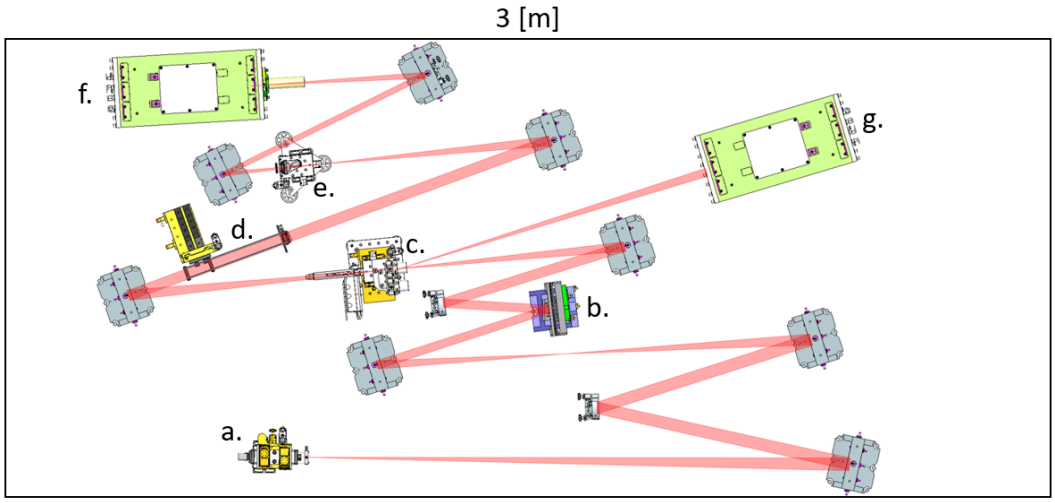


Figure 1: As shown in (Noyes_2023), the CAD model of the DST2. The black border represents the perimeter of the optical table. Components labeled include: a. the source assembly, b. A BMC MEMs 2K DM, c. The focal plane mask (FPM) assembly, d. The Lyot stop assembly, e. The field stop assembly, f. The Science camera, and g. The Wavefront Sensing Camera (not used during spectral LDFC experiments).

In order to switch between the sensing band and the science band, a supercontinuum broadband laser (NKT Photonics SuperK FIANIUM (NKT Photonics, Fianium, 2023) is fed through a photonic crystal fiber (PCF) supporting a large spectral bandwidth, to a variable bandwidth monochromator with a 440 nm wide tuning range and variable bandwidth (NKT Photonics, Varia, 2023). The variable filter allows us to switch between spectral bands in approximately 1 second. We used a step-index single-mode fiber to connect the output of the monochromator to the input of the coronagraph, which leads to a large reduction in flux at wavelengths longer than 650 nm. Ideally, the separation between the science and sensing bands should be as large as possible, but we were limited by the bandwidth of the single-mode fiber. For these experiments, we used a science band center wavelength of $\lambda_{sci} = 530\,nm$ and a sensing band center wavelength of $\lambda_{sens} = 650\,nm$. Both bands have a fractional bandwidth of $\Delta\lambda/\lambda = 0.01$.

For these experiments, the DST2 was configured with a Lyot focal plane mask (FPM). We also used a single 50 X 50 actuator microelectromechanical (MEMS) DM manufactured by Boston Micromachines. These DMs exhibit no hysteresis when switching between commanded patterns. The physical field stop (FS) used for this experiment has an outer edge of approximately 12.4 $\lambda_{sci}/D$ and an inner edge of approximately 2.5 $\lambda_{sci}/D$.

The science camera, which is used for acquiring the science and sensing band images, is an Andor NEO sCMOS camera. This camera has a 6.5 μm pitch $2160 \times 2560$ pixel array. For these experiments, acquiring the full frame is unnecessary so we only readout a 500 x 500 sub-image from the camera. The camera is not vacuum rated, which required us to enclose the camera in a pressurized vessel. A broadband window is used to transmit light to the camera.

## Experimental Overview: Creating the dark hole region

We first establish a broadband DH before creating a monochromatic DH. In our experience, Lyot Coronagraphs tend to be less sensitive to tip and tilt wavefront error when using multiple sub-bands during EFC. We do not fully understand this but exploration of this effect is outside the scope of this SAT.

We used the FALCO software library (Riggs et al 2018) which employs PWP and EFC to create a 10% bandwidth DH around the science band center wavelength (530 nm) with 5 sub-bandpasses. This takes 100 iterations and approximately 18 hours. Using the DM solution for the broadband DH as a starting point, we then created a monochromatic (1% fractional bandwidth) DH using 5-10 iterations of PWP and EFC. We are able to reach NI levels of a few E-9. An example of the science band DH is shown in Fig. 2 (left), with the correction region used by EFC shown inside the red outline. Once the desired NI in the science band DH is established, we store the DM command corresponding to this high contrast DH. The DH was created over a single side of the focal plane mask (180 deg), as a single DM was used for speckle control. This limitation is inherent to single-DM correction; a 360-deg DH created with two DMs would be also be suitable for spectral LDFC.

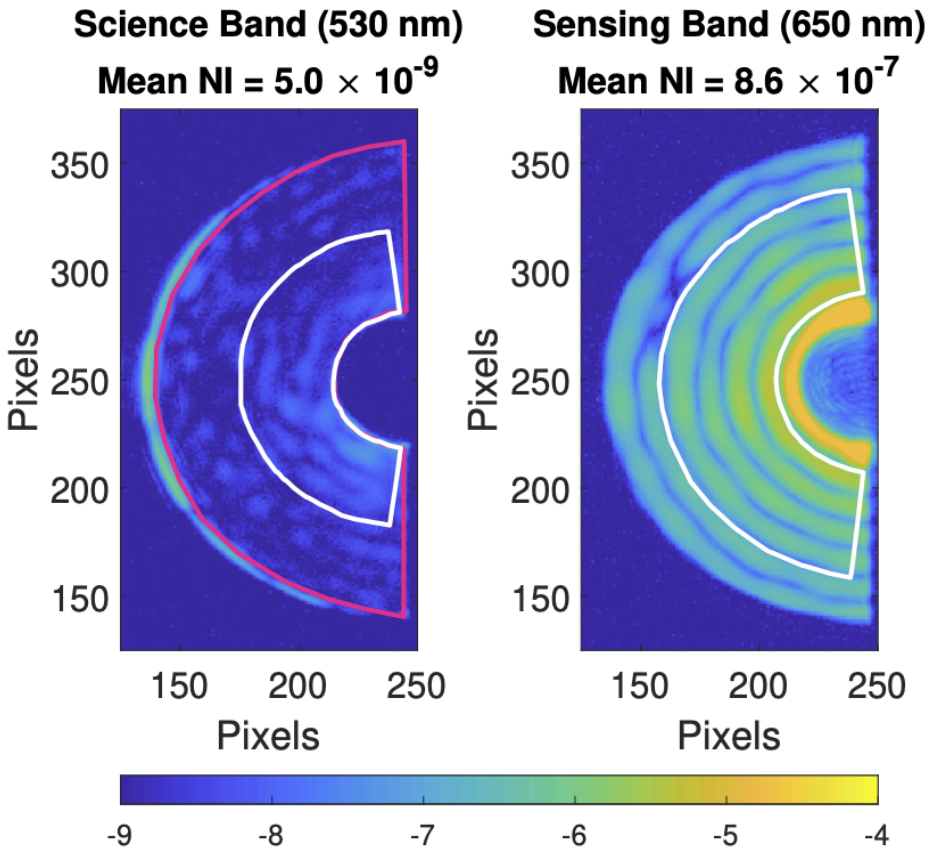


Figure 2. The science band NI image (left) after creating a DH with several iterations of PWP and EFC. The red outline denotes the correction regions for EFC. The white outline denotes the science band mask. The sensing band NI image (right) for the same DM pattern. The white outline denotes the sensing band mask. The quoted mean NI in this figure is based on the mean image of ten

exposures, each lasting 10 seconds. The raw 500x500 pixel images have been cropped to show here and in subsequent figures a rectangular area including the C-shaped focal plane field stop.

## Experimental Overview: Linearity in the sensing band

For spectral LDFC, the bright field (sensing band), the mean NI is several orders of magnitude larger than in the science band (see Fig. 2, right ). To satisfy that we are in the linear range, we placed sine wave patterns on the DM that correspond to localized speckle inside both the sensing and science band masks. The zero-crossing of the sine function was set in the center of the 50x50 DM actuator grid, between the 25th and 26th actuators. We then vary the amplitude of the sine wave from -20 mV to 20 mV peak-to-valley (or approximately $\pm$0.2 nm PTV). The corresponding NI of the speckle generated on the focal plane is recorded and the NI from the unprobed image is subtracted. Figure 3 shows the change in NI at several different pixel locations, the same color for the left and right plots are for the same spatial location scaled by their respective wavelength. There is a clear quadratic response to the sine wave amplitude in the science band while in the sensing band, the response is approximately linear and monotonic for small amplitudes (-10 mV to 10 mV).

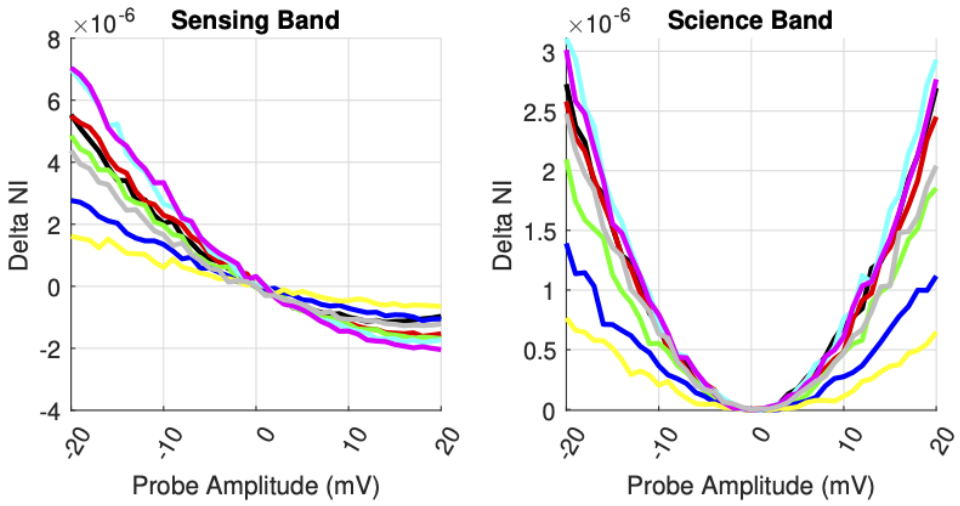


Figure 3. Experimentally measured ΔNI (NI of the probed image location - NI of unprobed image location) for several spatial locations in the sensing band (left) and the science band DH (right). The same color in both plots correspond to the same respective location in units of $\lambda/D$. This demonstrates the approximately linear response, over this probe amplitude range, in the sensing band compared to the science band which exhibits a quadratic response. The $\sim\pm$20 mV probe amplitude range corresponds to $\pm$0.2 nm PTV in DM surface height.

## Experimental Overview: Calibration

The spectral LDFC calibration procedure empirically measures the change in NI in the sensing band for each mode of the DM poke basis. The corresponding measurements are stored as columns in the N × M response matrix $\mathbf{R}$, where N is the number of evaluation pixels in the sensing band focal plane area and M is the number of DM poke modes (not necessarily orthogonal at this point).

Prior to beginning the calibration we generated the science and sensing band masks. First we specify the science band mask such that it is inside the DH region created with PWP and EFC. The initial sensing

band mask shown in Fig. 4 (left) has the same dimensions as the science band as measured by angular coordinates ($\lambda/D$). Therefore any speckles that we place on the sensing band will show up at the same location in the science band, scaled by their respective wavelength.

In the second step, a non-linear pixel rejection mask is created (see in Fig. 4 right). Pixels with low NI in the unprobed image are more likely to exhibit a non-linear response to changes in wavefront. Here, we consider only the pixels inside the initial sensing band mask. Pixels whose NI values are lower than a threshold times the median of the sensing band NI are rejected. For the results shown in this paper we used a threshold value of 0.6 - 0.7.

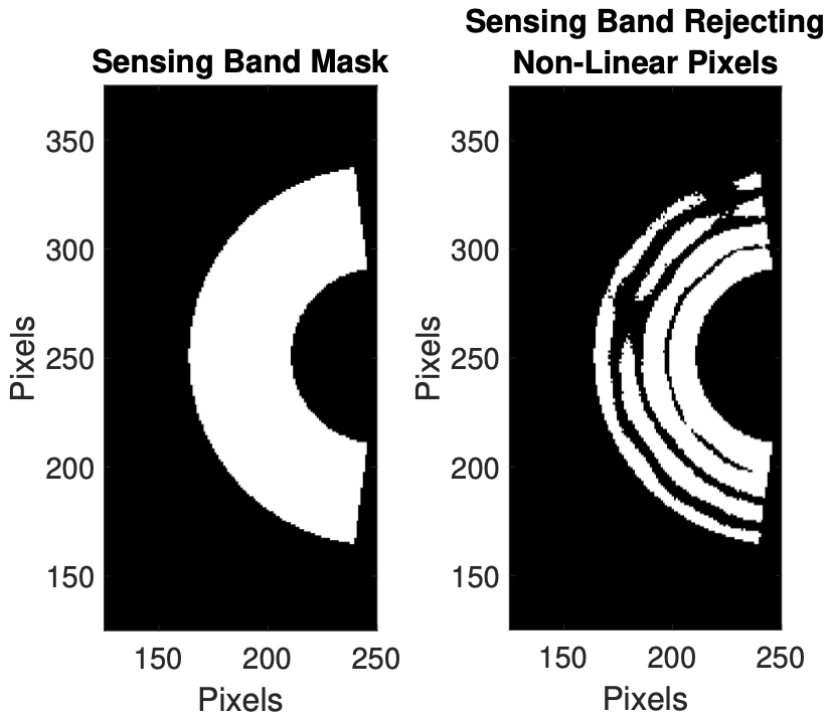


Figure 4. Initial sensing band mask (left), the science band mask has an equivalent shape. The inner radius is 3.7 $\lambda/D$ and outer radius is 8 $\lambda/D$ with an angular width of 165 degrees. The actual sensing band mask (right) is a subset of the original sensing band pixel mask, designed to reject spatial locations with a non-linear pixel response.

The next step is to choose a DM poke basis for the calibration. There are several possible bases to choose from such as the actuator basis (individual actuators), Hadamard basis, or sines wave patterns. We decided against using the actuator basis as it is time consuming and produces low SNR. Using the Hadamard basis increases the SNR but requires as many exposures as the actuator basis, which for our case is 2500. For these reasons we chose to use the sine wave basis which allows us to place high SNR speckle in the science and sensing band. We precomputed the sine wave DM patterns to spatially overfill the sensing band pixel mask with speckle spaced 1 ($\lambda/D$) apart in a square grid pattern.

During each iteration of the calibration loop, a positive and negative amplitude sine wave (positive and negative probe) is applied to the DM. Only measurements from the sensing band are required. The images from the positive probe and the negative probe are subtracted and scaled by the reciprocal of twice the amplitude:

$$\mathbf{R}_m = \frac{1}{2A}\left(\mathbf{n}_m^+ - \mathbf{n}_m^-\right)$$

where $\mathbf{n}_m^+$ is the vectorized sensing band image associated with the positive probe for the m[th] basis vector and $\mathbf{n}_m^-$ is associated with the negative probe, both are N x 1 vectors. A is the amplitude of the probe which in our case is 10 mV (approx. 0.1 nm PTV), to remain in the linear range. The resulting vector $\mathbf{R}_m$ is placed in the m[th] column of $\mathbf{R}$. Therefore $\mathbf{R}$ is an N x M matrix, where N is the number of pixels in the sensing band pixel mask and M is the number of modes (basis vectors) used during the calibration.

During each iteration of the calibration, we iteratively add to the reference measurement vector

$$\mathbf{n}_{ref} = \frac{1}{2M}\sum_{m=1}^{M}\left(\mathbf{n}_m^+ + \mathbf{n}_m^-\right)$$

where $\mathbf{n}_m^+$ and $\mathbf{n}_m^-$ is an N × 1 vector.

## Experimental Overview: Wavefront sensing and control loop

In spectral LDFC, the forward model can be summarized as

$$\Delta\mathbf{n} = \mathbf{R}\Delta\mathbf{w}$$

where $\Delta\mathbf{n}$ is the change in NI in the sensing band pixel mask and $\Delta\mathbf{w}$ is the change in wavefront relative to the initial DH wavefront. Thus, we can extend this concept to a WFSC loop by denoting the measurement in the k[th] iteration as the difference between current sensing band NI vector and the reference sensing band NI vectors

$$\Delta\mathbf{n}_k = \mathbf{n}_k - \mathbf{n}_{ref},$$

Where each $\mathbf{n}_k$ is an N x 1 vectorized measurement of NI inside the sensing band pixel mask at iteration k.

The modal control approach allows us to extend the singular value decomposition (SVD) pseudoinverse for more precise control of each eigenmode during the spectral LDFC WFSC loop:

$$\mathbf{x}_k = \mathbf{L}(\mathbf{x}_{k-1} - \mathbf{G}\boldsymbol{\Sigma}^{\dagger}\mathbf{U}^T\Delta\mathbf{n}_k),$$

here $\mathbf{x}_k$, an M x 1 vector, is the control command per eigenmode. $\mathbf{G}$ is the modal gain, a diagonal matrix with elements $\mathbf{g}_m$ and $\mathbf{L}$ is the modal leak, a diagonal matrix with elements 1 - $l_m$. The leak values $l_m$ are a multiplicative factor used to drive commands to zero, implementing a leaky integrator control law.

Leaks were only applied for control modes >#50 as a way to turn control off, and that no leak was applied on modes 1-50, which were controlled with full gain=1. The control law equation is shown in the equation above and also under the box labeled “Control command in eigenmode basis” in Figure 5. We note that the leak coefficient is applied AFTER the gain, so a mode with L=0 will always have a zero command applied.

To complete the loop and apply the correction to the DM, we compute the correction in the calibration basis we originally used to acquire the response matrix

$$\mathbf{f}_k = \mathbf{V}\mathbf{x}_k$$

where $\mathbf{f}_k$ an M x 1 vector. Then multiply by $\mathbf{D}$ to convert to the actuator basis. Thus the control command in the actuator basis is

$$\mathbf{p}_k = \mathbf{D}\mathbf{f}_k$$

where the columns of $\mathbf{D}$ are the sine wave patterns from calibration. $\mathbf{D}$ is an $N_{act}$ x M matrix. $N_{act}$ is the number of actuators across the DM assuming a square actuator pattern. $\mathbf{f}_k$ is an $N_{act}^2$ x 1 vector.

The spectral LDFC WFSC loop is summarized in Fig. 5. This figure and equations above show that the operations involved are mostly matrix multiplications.

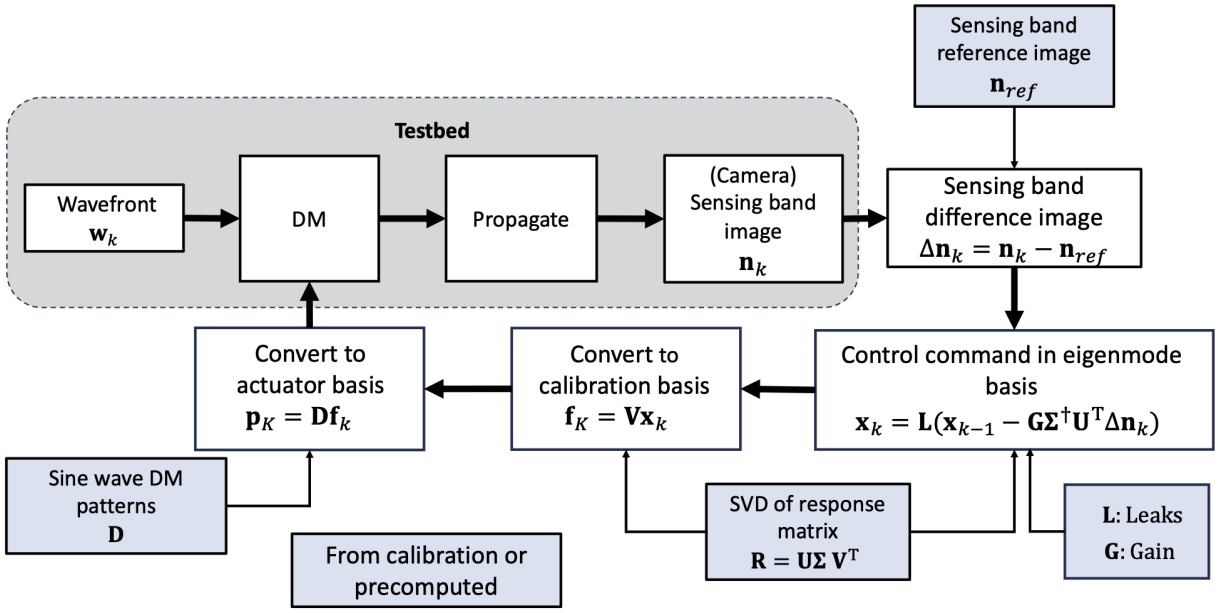


Figure 5: The spectral LDFC wavefront sensing and control loop. Note there is no requirement to use the science band. The boxes within the gray area represent physical components or processes on the testbed. The light blue boxes are quantities that are precomputed or known prior to the spectral LDFC WFSC loop.

# Experimental Results

We conducted multiple demonstrations of spectral LDFC on the DST2 testbed. We used PWP and EFC to establish a DH with starting contrasts from ~1E-9 to ~6E-9 NI in the science band scoring region

established by the pixel mask in Fig 4. We then applied a linear combination of eigenmodes of the response matrix as a disturbance,

$$\mathbf{w} = \sum_i a_i \mathbf{v}_i$$

where $a_i$ is the amplitude and $v_i$ is the $i^{th}$ eigenmode of the response matrix. The simulated DM surface pattern for the first 10 eigenmodes is shown in Fig 6. and the corresponding simulated science band images are shown in Fig 7.

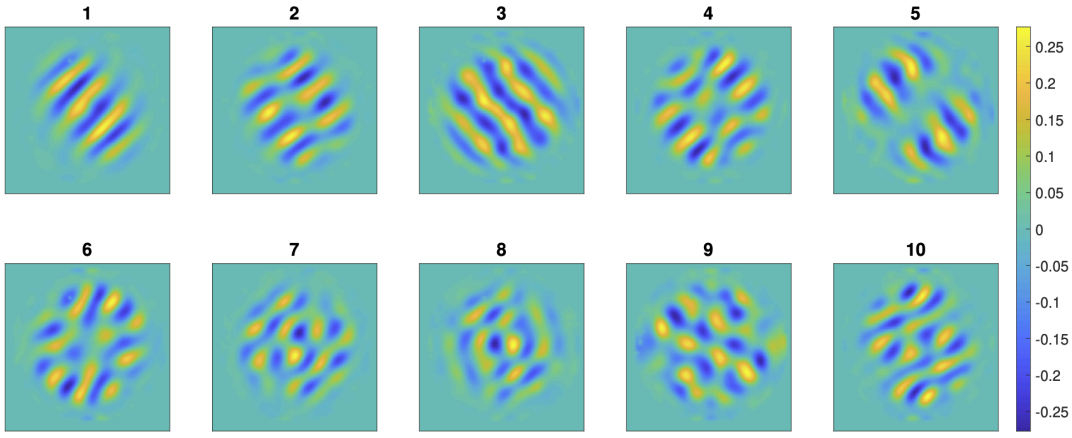


Figure 6. The simulated DM surface, in nanometers, for the first 10 (out of 116) eigenmodes for the response matrix for the sensing band. The response matrix are fourier modes for a correction region that corresponds to 3.7 to 8 λ /D with an angular width of 165 degrees. These images only show the DM surface due to the eigenmode, not the total DM surface pattern which would include the DM surface responsible for generating the dark hole.

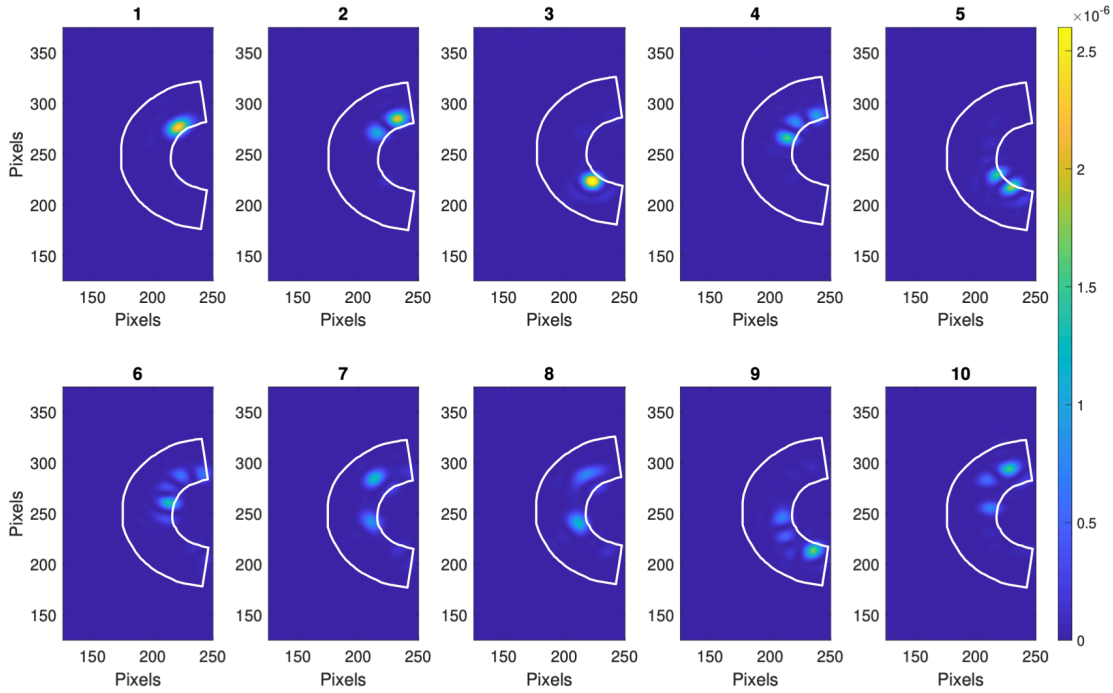


Figure 7. The simulated science band images corresponding to the first 10 (of out 116) eigenmodes for the response matrix for the sensing band correction region corresponding to 3.7 to 8 λ/D with an angular width of 165 degrees. The white outline represents the pixel mask which is the scoring region. These images only show the intensity due to the eigenmode, not the total intensity field which would include the component from the dark hole.

## An example demonstration of Spectral LDFC

One particular demonstration of spectral LDFC is shown in Fig 8, 9, 10 where we applied the first seven eigenmodes with an amplitude $a_i$ of 20 mV (approx 0.2 nm Peak-To-Valley). This is twice the amplitude we used for the sine wave basis during the calibration. This degraded the mean NI in the science band scoring region to 9.8E-7, as seen in Fig 8 (center).

We then applied the spectral LDFC algorithm as explained in earlier. Figure 10 shows a plot of both the closed-loop and open-loop performance. The red line is the mean NI in the science band mask without the correction applied. The blue line is the mean NI with the correction applied. The plot shown in Fig. 10 is from a single exposure at 1 second integration times per control iteration for both the science and sensing band to reduce the duration of the WFSC experiment; the same coronagraph would require 60 second integration time per control iteration with EFC alone. After nine control iterations, the closed-loop mean NI improved to less than E-8. After 120 control iterations, the corrected science band mean NI is slightly worse than the starting value, as seen in Fig. 8 (right). In the final iteration, the closed loop mean NI shows a factor of over 170x improvement compared the open loop mean NI.

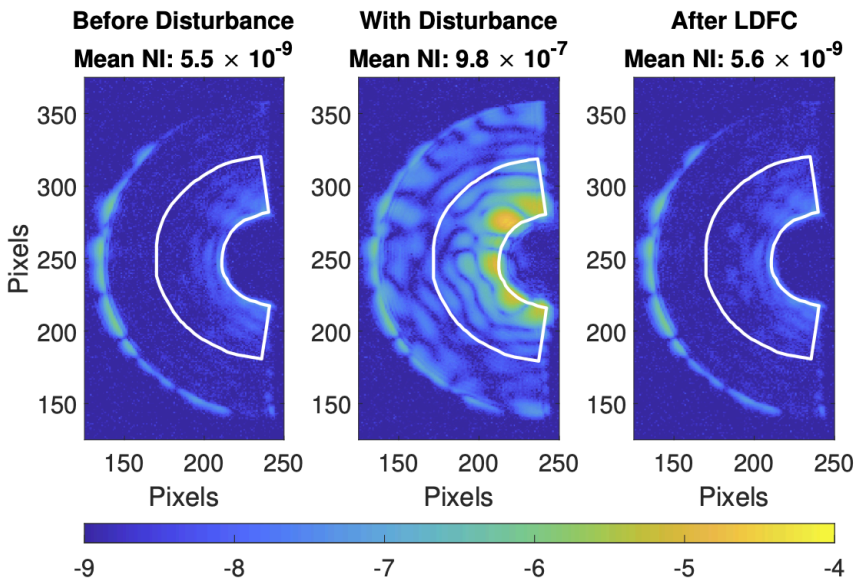


Figure 8. The science band image ($\log_{10}$ NI) (left)~before a disturbance is injected using the DM and (center) with a disturbance composed of the first seven eigenmodes applied to the DM. The mean NI over the science band mask is 100 times larger than the initial mask. (Right) The science band image after 120 iterations of spectral LDFC and modal control, the science band image mean NI has been corrected to slightly larger than the original value of 5.5E-9. The white outline shows the science band pixel mask in which we use to score the mean NI in the science band. Each image is the average of 10 images at 10 second exposure time. For this figure, the mean NI is computed from the averaged image over the science band mask.

The difference between the after LDFC image and the before disturbance image is shown in Fig. 9. To compute the inherent RMS in the difference image inside the science band mask one must remove the effect due to noise. The RMS is calculated as $RMS_{diff} = (RMS_{total}^2 - RMS_{noise}^2)^{½}$, where $RMS_{diff}$ is the inherent RMS in the difference image, $RMS_{total}$ is the combined RMS from both the underlying difference image and noise, and $RMS_{noise}$ is the RMS of a 150x150 pixels corner where the FS is opaque.

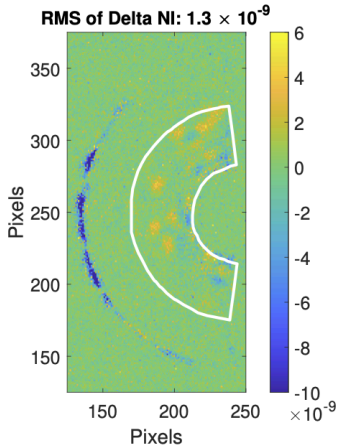


Figure 9. The difference of the two science band averaged images from Fig 8: after LDFC minus before disturbance, denoted as Delta NI. The color scale is a linear color scale. The root-mean-square (RMS) of

the Delta NI in the science band mask is 1.3E-9. The RMS is computed over the science band mask, denoted by the white outline.

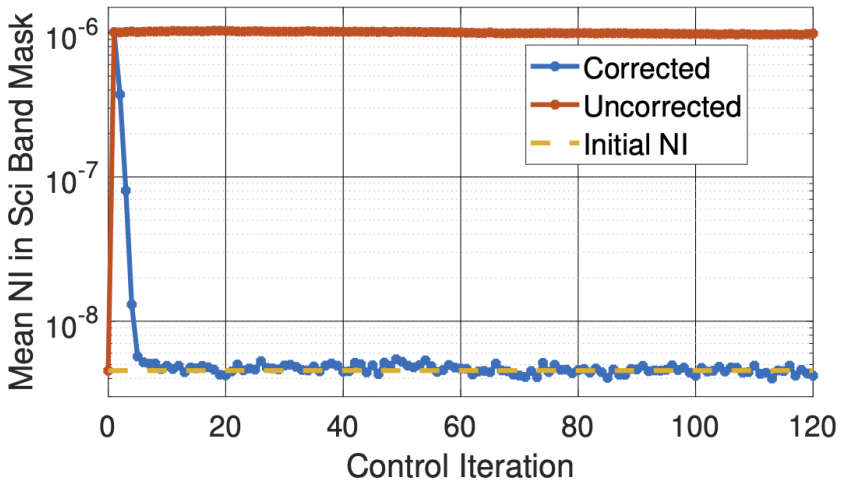


Figure 10. Mean NI during the 120 iterations of spectral LDFC with modal control. The first seven eigenmodes of the response matrix are equally injected with the same amplitude, 20 mV, as a disturbance. The blue line is the mean NI in the science band mask with the correction as computed from modal control, applied to the DM. After 10 iterations the science band mean NI has been corrected. Spectral LDFC successfully detects and corrects the disturbances to nearly the original mean NI in the science band. The red line is the mean NI in the science band mask without any correction applied. The dashed yellow line shows the mean NI before the disturbance is injected to serve as a useful visual indicator.

## Tuning the leaks for modal control

We heuristically chose the leak values by observing how the lack of leaks affects the control (see Fig. 11, bottom). Without any leaks, the modal control algorithm attempted to control eigenmodes 50 and higher even though they were not added as synthetic disturbances. This caused the control loop to diverge after 6 iterations (see Fig. 12 yellow line plot). As we increased the strength of those leaks, both the control (see Fig. 11, middle and top) and the DH NI versus iteration became more stable (see Fig. 12 red and blue).

For the results shown in Fig. 10 and Fig. 8, we used leak values of $l_m$ = 0.6 for eigenmodes 50 to 59 and turned off control $l_m$ = 1.0 for eigenmodes 60 to 116 (there are 116 eigenmodes). We noticed that eigenmodes 60 and higher were being controlled even though there was no disturbance being applied to them, this was causing the science band mean NI to drift. The higher eigenmodes tend to have lower SNR and higher cross-talk. Higher order eigenmodes also tend to have higher spatial frequencies which are more difficult to realize on a deformable mirror.

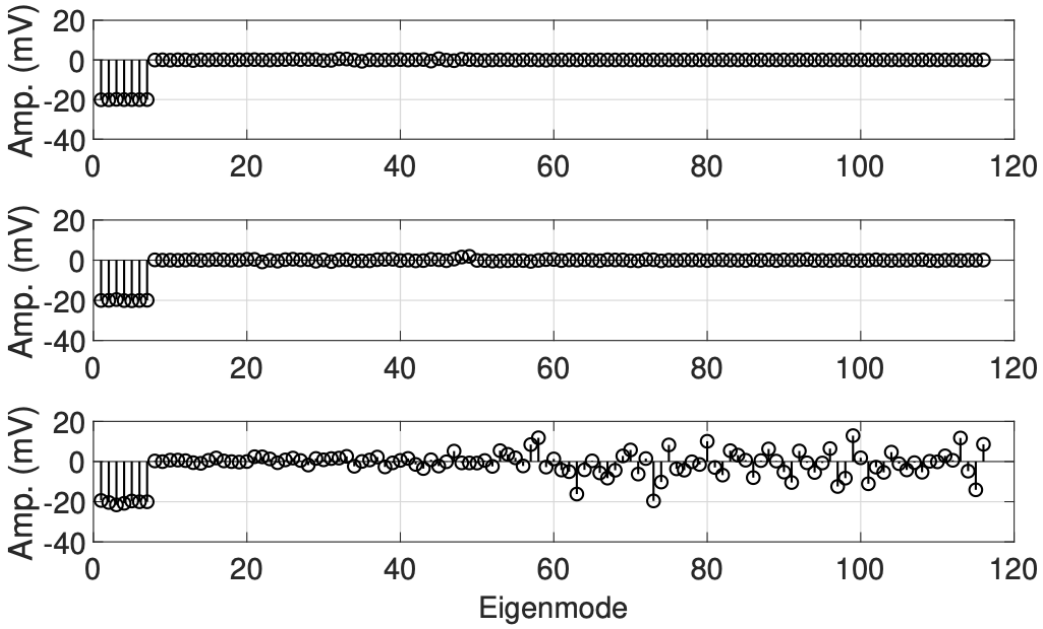


Figure 11: (Top) The control for each eigenmode at iteration k=10 with a leak value of 0.6 for eigenmodes 50-59 and 1.0 for eigenmodes 60 and higher. (Middle) The control also at iteration $k=10$ but with a leak value set to 0.3 for eigenmodes 50-59 and 0.6 for eigenmodes 60 and higher. (Bottom) The control also at iteration $k=10$ but when all the leak values set to 0.

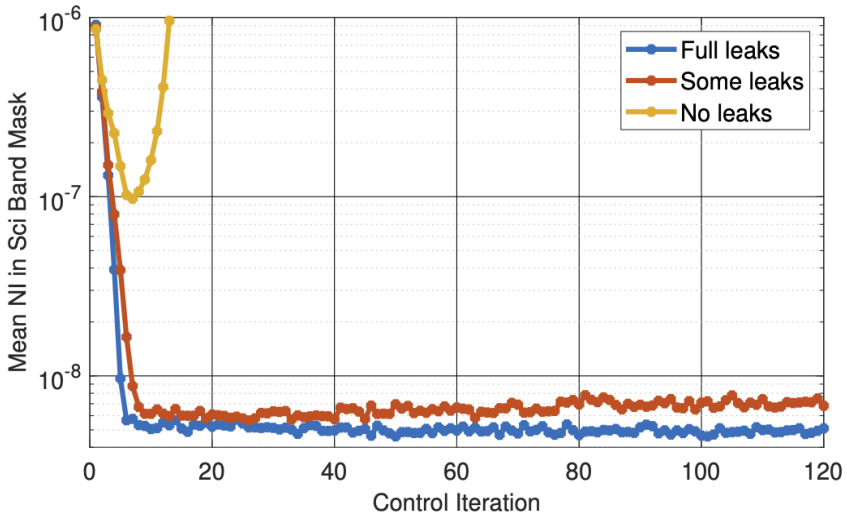


Figure 12: (Blue) The mean NI in the science band for a leak value of 0.6 for eigenmodes 50-59 and 1.0 for eigenmodes 60 and higher. (Red) The mean NI in the science band for a leak value 0.3 for eigenmodes 50-59 and 0.6 for eigenmodes 60 and higher. (Yellow) The mean NI in the science band when all the leak values set to 0.

# Addressing Specific Milestone 2 Requirements

- **Demonstrate a 10x suppression of injected disturbances by use of spectral LDFC stabilization in a dark hole with area covering at least 10 sq-lambda/D and reaching a raw**

**contrast (post-LDFC) level below 1e-7:** Each of the experiments in Table 1 demonstrated this ability using various linear combinations of eigenmodes as an injected disturbance.

- **Measurements will be performed in the visible to the near NIR, 400 nm to 1700 nm**: For each experiment listed in Table 1, the science center wavelength was set to 530 nm with a 1% bandwidth and the sensing center wavelength was set to 650 nm with a 1% bandwidth.
- **The Dark Field and Bright Field spectral bands will be non-overlapping, and sufficiently separated to ensure high efficient spectral LDFC operation:** For each experiment listed in Table 1, the science center wavelength was set to 530 nm with a 1% bandwidth and the sensing center wavelength was set to 650 nm with a 1% bandwidth. As shown in Fig. 2, the bright field which we denote the sensing band typically has several orders of magnitude more flux than the science band at the initial dark hole DM state.
- **The scoring area shall be within the primary control region of the deformable mirrors:** For each experiment we use only one deformable mirror. The primary control region used during PWP and EFC was set from 3.5 $\lambda_{sci}$/D to 12.4 $\lambda_{sci}$/D for a 180 degree DH. As shown in Table 1, the minimum inner radius, across all experiments, of the scoring area was 3.5 $\lambda_{sci}$/D, the maximum outer radius was 8.0 $\lambda_{sci}$/D, and the maximum angular width was 170 degrees.
- **The raw contrast shall be measured as the surface brightness averaged over a fixed area covering at least 10 square lambda/D:** For each experiment in Table 1, the NI is the average over the science band scoring region. Each of which covers an area of at least 10 sq $\lambda_{sci}$/D.
- **For all measurements, the raw contrast shall be < 1E-7 (average) both without dynamic errors prior to LDFC, and with dynamic errors plus LDFC. Wavefront errors may need to be applied to demonstrate the LDFC gain, in which case the exact same sequence of aberrations shall be introduced for the ON and OFF sequences to be compared:** Each static disturbance experiment in Table 1 shows we had a starting raw contrast of < 1E-7 in the science band scoring region before static disturbances were added. Dynamic errors were injected in a separate set of measurements performed in air before moving the test in vacuum, as detailed in Table 2, with contrast evolution shown in figures following Table 2.

| LDFC Exp Label # | Date | Starting Science Band Scoring Region Contrast (Mean NI) | Aberrated Science Band Scoring Region Contrast (Mean NI) | Post LDFC Contrast, Science Band Scoring Region (Mean NI) | Scoring Region Inner Radius ($\lambda_{sci}$/D) | Scoring Region Outer Radius ($\lambda_{sci}$/D) | Scoring Region Angular Width (Degrees) | Science Band Scoring Region Area ($\lambda_{sci}/D)^2$ | Aberrations Injected | Control Iterations after aberration injected | Improvement Ratio Last 100 Iterations (Scoring Region) |
|---|---|---|---|---|---|---|---|---|---|---|---|
| 11 | 2023-07-26 | 4.15E-09 | 1.15E-07 | 1.07E-08 | 3.50 | 8.00 | 25.00 | 11.29 | First Eigenmode with amplitude of 0.9 | 120 | 13.74 |
| 14 | 2023-0727 | 1.82E-09 | 7.68E-08 | 3.73E-09 | 3.50 | 8.00 | 25.00 | 11.29 | First Eigenmode with amplitude of 0.7 | 120 | 20.36 |
| 18 | 2023-07-29 | 2.92E-09 | 6.40E-08 | 3.11E-09 | 3.50 | 8.00 | 25.00 | 11.29 | First Eigenmode with amplitude of 0.6 | 120 | 16.45 |
| 25 | 2023-07-29 | 2.94E-09 | 6.34E-08 | 4.44E-09 | 3.50 | 8.00 | 25.00 | 11.29 | First Eigenmode with amplitude of 0.6 | 120 | 14.21 |
| 26 | 2023-07-29 | 2.57E-09 | 6.14E-08 | 4.09E-09 | 3.50 | 8.00 | 25.00 | 11.29 | First Eigenmode with amplitude of 0.6 | 120 | 15.23 |
| 27 | 2023-07-30 | 2.30E-09 | 5.63E-08 | 3.01E-09 | 3.50 | 8.00 | 25.00 | 11.29 | First Eigenmode with amplitude of 0.6 | 120 | 15.70 |

| | | | | | | | | | | | |
|---|---|---|---|---|---|---|---|---|---|---|---|
| 28 | 2023-07-30 | 2.55E-09 | 6.23E-08 | 4.65E-09 | 3.50 | 8.00 | 25.00 | 11.29 | First Eigenmode with amplitude of 0.6 | 120 | 14.34 |
| 29 | 2023-07-30 | 2.49E-09 | 6.61E-08 | 4.50E-09 | 3.50 | 8.00 | 25.00 | 11.29 | First Eigenmode with amplitude of 0.6 | 120 | 14.01 |
| 30 | 2023-07-30 | 2.18E-09 | 6.34E-08 | 4.60E-09 | 3.50 | 8.00 | 25.00 | 11.29 | First Eigenmode with amplitude of 0.6 | 120 | 13.74 |
| 31 | 2023-07-30 | 2.20E-09 | 6.24E-08 | 4.29E-09 | 3.50 | 8.00 | 25.00 | 11.29 | First Eigenmode with amplitude of 0.6 | 120 | 14.53 |
| 32 | 2023-07-30 | 2.27E-09 | 5.72E-08 | 4.15E-09 | 3.50 | 8.00 | 25.00 | 11.29 | First Eigenmode with amplitude of 0.6 | 120 | 15.29 |
| 33 | 2023-07-30 | 2.87E-09 | 6.25E-08 | 5.36E-09 | 3.50 | 8.00 | 25.00 | 11.29 | First Eigenmode with amplitude of 0.6 | 120 | 13.96 |
| 34 | 2023-07-30 | 2.74E-09 | 6.26E-08 | 4.57E-09 | 3.50 | 8.00 | 25.00 | 11.29 | First Eigenmode with amplitude of 0.6 | 120 | 13.67 |
| 35 | 2023-07-30 | 1.80E-09 | 6.25E-08 | 4.01E-09 | 3.50 | 8.00 | 25.00 | 11.29 | First Eigenmode with amplitude of 0.6 | 120 | 14.79 |
| 37 | 2023-07-30 | 2.74E-09 | 6.02E-08 | 4.36E-09 | 3.50 | 8.00 | 25.00 | 11.29 | First Eigenmode with amplitude of 0.6 | 120 | 14.40 |
| 39 | 2023-07-30 | 2.33E-09 | 5.64E-08 | 4.83E-09 | 3.50 | 8.00 | 25.00 | 11.29 | First Eigenmode with amplitude of 0.6 | 120 | 14.33 |
| 40 | 2023-07-30 | 2.73E-09 | 6.38E-08 | 5.31E-09 | 3.50 | 8.00 | 25.00 | 11.29 | First Eigenmode with amplitude of 0.6 | 120 | 13.16 |
| 41 | 2023-07-30 | 2.57E-09 | 6.19E-08 | 4.80E-09 | 3.50 | 8.00 | 25.00 | 11.29 | First Eigenmode with amplitude of 0.6 | 120 | 14.55 |
| 42 | 2023-07-30 | 1.93E-09 | 5.54E-08 | 3.50E-09 | 3.50 | 8.00 | 25.00 | 11.29 | First Eigenmode with amplitude of 0.6 | 120 | 16.18 |
| 43 | 2023-07-30 | 2.79E-09 | 6.43E-08 | 4.53E-09 | 3.50 | 8.00 | 25.00 | 11.29 | First Eigenmode with amplitude of 0.6 | 120 | 14.80 |
| 44 | 2023-07-30 | 2.49E-09 | 6.26E-08 | 5.34E-09 | 3.50 | 8.00 | 25.00 | 11.29 | First Eigenmode with amplitude of 0.6 | 120 | 13.78 |
| 45 | 2023-07-30 | 2.36E-09 | 6.18E-08 | 3.68E-09 | 3.50 | 8.00 | 25.00 | 11.29 | First Eigenmode with amplitude of 0.6 | 120 | 13.81 |
| 46 | 2023-07-30 | 2.74E-09 | 5.65E-08 | 3.72E-09 | 3.50 | 8.00 | 25.00 | 11.29 | First Eigenmode with amplitude of 0.6 | 120 | 14.20 |
| 47 | 2023-07-30 | 2.02E-09 | 6.22E-08 | 4.67E-09 | 3.50 | 8.00 | 25.00 | 11.29 | First Eigenmode with amplitude of 0.6 | 120 | 13.29 |
| 48 | 2023-07-30 | 2.72E-09 | 5.51E-08 | 3.97E-09 | 3.50 | 8.00 | 25.00 | 11.29 | First Eigenmode with amplitude of 0.6 | 120 | 15.35 |
| 49 | 2023-07-30 | 2.54E-09 | 5.22E-08 | 4.10E-09 | 3.50 | 8.00 | 25.00 | 11.29 | First Eigenmode with amplitude of 0.6 | 120 | 13.53 |
| 50 | 2023-07-30 | 2.61E-09 | 5.54E-08 | 3.97E-09 | 3.50 | 8.00 | 25.00 | 11.29 | First Eigenmode with amplitude of 0.6 | 120 | 14.92 |
| 51 | 2023-07-30 | 1.98E-09 | 5.59E-08 | 4.84E-09 | 3.50 | 8.00 | 25.00 | 11.29 | First Eigenmode with amplitude of 0.6 | 120 | 13.40 |
| 52 | 2023-07-30 | 3.06E-09 | 6.20E-08 | 4.46E-09 | 3.50 | 8.00 | 25.00 | 11.29 | First Eigenmode with amplitude of 0.6 | 120 | 14.13 |
| 53 | 2023-07-30 | 2.02E-09 | 6.20E-08 | 4.97E-09 | 3.50 | 8.00 | 25.00 | 11.29 | First Eigenmode with amplitude of 0.6 | 120 | 13.37 |
| 54 | 2023-07-30 | 1.92E-09 | 6.36E-08 | 4.26E-09 | 3.50 | 8.00 | 25.00 | 11.29 | First Eigenmode with amplitude of 0.6 | 120 | 13.14 |

| | | | | | | | | | | | |
|---|---|---|---|---|---|---|---|---|---|---|---|
| 55 | 2023-07-30 | 2.25E-09 | 6.25E-08 | 5.54E-09 | 3.50 | 8.00 | 25.00 | 11.29 | First Eigenmode with amplitude of 0.6 | 120 | 14.00 |
| 56 | 2023-07-30 | 2.30E-09 | 5.66E-08 | 3.99E-09 | 3.50 | 8.00 | 25.00 | 11.29 | First Eigenmode with amplitude of 0.6 | 120 | 15.01 |
| 57 | 2023-07-30 | 2.11E-09 | 6.26E-08 | 3.96E-09 | 3.50 | 8.00 | 25.00 | 11.29 | First Eigenmode with amplitude of 0.6 | 120 | 13.86 |
| 58 | 2023-07-30 | 2.31E-09 | 6.17E-08 | 4.48E-09 | 3.50 | 8.00 | 25.00 | 11.29 | First Eigenmode with amplitude of 0.6 | 120 | 13.82 |
| 59 | 2023-07-31 | 2.24E-09 | 6.07E-08 | 5.02E-09 | 3.50 | 8.00 | 25.00 | 11.29 | First Eigenmode with amplitude of 0.6 | 120 | 13.54 |
| 60 | 2023-07-31 | 2.38E-09 | 5.53E-08 | 3.39E-09 | 3.50 | 8.00 | 25.00 | 11.29 | First Eigenmode with amplitude of 0.6 | 120 | 15.68 |
| 61 | 2023-07-31 | 2.79E-09 | 6.21E-08 | 5.16E-09 | 3.50 | 8.00 | 25.00 | 11.29 | First Eigenmode with amplitude of 0.6 | 120 | 12.70 |
| 62 | 2023-07-31 | 2.17E-09 | 6.16E-08 | 3.99E-09 | 3.50 | 8.00 | 25.00 | 11.29 | First Eigenmode with amplitude of 0.6 | 120 | 14.71 |
| 63 | 2023-07-31 | 2.24E-09 | 6.07E-08 | 3.27E-09 | 3.50 | 8.00 | 25.00 | 11.29 | First Eigenmode with amplitude of 0.6 | 120 | 13.54 |
| 64 | 2023-07-31 | 2.38E-09 | 6.22E-08 | 3.95E-09 | 3.50 | 8.00 | 25.00 | 11.29 | First Eigenmode with amplitude of 0.6 | 120 | 14.48 |
| 65 | 2023-07-31 | 2.79E-09 | 5.66E-08 | 2.92E-09 | 3.50 | 8.00 | 25.00 | 11.29 | First Eigenmode with amplitude of 0.6 | 120 | 15.89 |
| 67 | 2023-07-31 | 2.12E-09 | 5.78E-08 | 2.92E-09 | 3.50 | 8.00 | 25.00 | 11.29 | First Eigenmode with amplitude of 0.6 | 120 | 15.40 |
| 68 | 2023-07-31 | 1.84E-09 | 9.41E-08 | 4.36E-09 | 3.50 | 8.00 | 25.00 | 11.29 | First Eigenmode with amplitude of 0.8 | 120 | 21.80 |
| 69 | 2023-07-31 | 1.77E-09 | 1.50E-07 | 4.44E-09 | 3.50 | 8.00 | 25.00 | 11.29 | First Eigenmode with amplitude of 1.0 | 120 | 24.47 |
| 70 | 2023-07-31 | 2.49E-09 | 1.52E-07 | 6.57E-09 | 3.50 | 8.00 | 25.00 | 11.29 | First Eigenmode with amplitude of 1.0 | 120 | 23.81 |
| 71 | 2023-07-31 | 2.09E-09 | 2.14E-07 | 4.96E-09 | 3.50 | 8.00 | 25.00 | 11.29 | First Eigenmode with amplitude of 1.2 | 120 | 30.83 |
| 73 | 2023-07-31 | 2.38E-09 | 3.01E-07 | 7.51E-09 | 3.50 | 8.00 | 25.00 | 11.29 | First Eigenmode with amplitude of 1.4 | 120 | 26.99 |
| 77 | 2023-07-31 | 2.37E-09 | 2.89E-07 | 1.06E-08 | 3.50 | 8.00 | 25.00 | 11.29 | First Eigenmode with amplitude of 1.4 | 120 | 73.87 |
| 78 | 2023-07-31 | 2.25E-09 | 2.91E-07 | 3.10E-09 | 3.50 | 8.00 | 25.00 | 11.29 | First Eigenmode with amplitude of 1.4 | 120 | 93.58 |
| 79 | 2023-07-31 | 2.26E-09 | 2.92E-07 | 3.14E-09 | 3.50 | 8.00 | 25.00 | 11.29 | First Eigenmode with amplitude of 1.4 | 120 | 89.54 |
| 80 | 2023-08-01 | 2.04E-09 | 3.03E-07 | 3.15E-09 | 3.50 | 8.00 | 25.00 | 11.29 | First Eigenmode with amplitude of 1.4 | 120 | 96.24 |
| 81 | 2023-08-01 | 2.82E-09 | 3.02E-07 | 2.98E-09 | 3.50 | 8.00 | 25.00 | 11.29 | First Eigenmode with amplitude of 1.4 | 120 | 80.30 |
| 82 | 2023-08-01 | 1.89E-09 | 3.14E-07 | 6.47E-09 | 3.50 | 8.00 | 25.00 | 11.29 | First Eigenmode with amplitude of 1.4 | 120 | 96.73 |
| 83 | 2023-08-01 | 2.72E-09 | 3.15E-07 | 3.78E-09 | 3.50 | 8.00 | 25.00 | 11.29 | First Eigenmode with amplitude of 1.4 | 120 | 97.26 |
| 84 | 2023-08-01 | 2.79E-09 | 3.03E-07 | 3.16E-09 | 3.50 | 8.00 | 25.00 | 11.29 | First Eigenmode with amplitude of 1.4 | 120 | 90.77 |

| | | | | | | | | | | | |
|---|---|---|---|---|---|---|---|---|---|---|---|
| 86 | 2023-08-01 | 2.24E-09 | 2.91E-07 | 3.49E-09 | 3.50 | 8.00 | 25.00 | 11.29 | First Eigenmode with amplitude of 1.4 | 120 | 67.17 |
| 87 | 2023-08-01 | 2.14E-09 | 3.03E-07 | 4.61E-09 | 3.50 | 8.00 | 25.00 | 11.29 | First Eigenmode with amplitude of 1.4 | 120 | 102.26 |
| 88 | 2023-08-01 | 2.07E-09 | 2.90E-07 | 3.25E-09 | 3.50 | 8.00 | 25.00 | 11.29 | First Eigenmode with amplitude of 1.4 | 120 | 91.83 |
| 123 | 2023-08-04 | 4.70E-09 | 9.57E-08 | 7.49E-09 | 3.50 | 8.00 | 170.00 | 76.77. | Eigenmodes 1-3 with amplitude 2.0 | 120 | 12.93 |
| 124 | 2023-08-04 | 4.83E-09 | 1.01E-07 | 5.11E-09 | 3.50 | 8.00 | 170.00 | 76.77 | Eigenmodes 1-3 with amplitude 2.0 | 120 | 19.28 |
| 136 | 2023-08-05 | 6.25E-09 | 3.98E-07 | 6.49E-09 | 3.70 | 8.00 | 165.00 | 72.44 | Eigenmodes 1-3 with amplitude 2.0 | 120 | 63.93 |
| 137 | 2023-08-05 | 6.78E-09 | 9.35E-07 | 6.44E-09 | 3.70 | 8.00 | 165.00 | 72.44 | Eigenmodes 1-7 with amplitude 2.0 | 120 | 142.30 |
| 142 | 2023-08-18 | 4.94E-09 | 9.08E-07 | 5.10E-09 | 3.70 | 8.00 | 165.00 | 72.44 | Eigenmodes 1-7 with amplitude 2.0 | 120 | 173.07 |
| 144 | 2023-08-18 | 4.77E-09 | 1.02E-06 | 1.00E-08 | 3.70 | 8.00 | 165.00 | 72.44 | Eigenmodes 1-7 with amplitude 2.0 | 120 | 153.92 |
| 145 | 2023-08-18 | 4.99E-09 | 8.76E-7 | 6.81E-09 | 3.70 | 8.00 | 165.00 | 72.44 | Eigenmodes 1-7 with amplitude 2.0 | 120 | 132.67 |
| 147 | 2023-08-23 | 6.0E-9 | 5.08E-07 | 7.33E-09 | 3.70 | 8.00 | 165.00 | 72.44 | Eigenmodes 1-3 with amplitude 2 | 120 | 74.33 |
| 157 | 2023-09-01 | 5.31E-9 | 9.19E-07 | 7.52E-09 | 3.70 | 8.00 | 165.00 | 72.44 | Eigenmodes 1-5 with amplitude 2 | 120 | 129.72 |

Table 1: Spectral LDFC Experiments which are denoted by Label number. Over 60 demonstrations of spectral LDFC were performed which meet the Milestone 2 requirements.

| Label | Date | #iterations | Injected disturbance | Post-LDFC contrast | Contrast gain factor |
|---|---|---|---|---|---|
| 84 | Nov 11, 2022 | 105 | Eigenmode #8 | 4.2e-8 | 10.4x |
| 85 | Nov 11, 2022 | 105 | Eigenmode #8 | 6.1e-8 | 11.2x |
| 125 | Dec 6, 2022 | 120 | Eigenmode #11 | 4.2e-8 | 11.3x |
| 129 | Dec 6, 2022 | 120 | Eigenmode #13 | 7.7e-8 | 14.09x |
| 145 | Dec 14, 2022 | 120 | Eigenmode #17 | 2.3e-8 | 18.09x |

Table 2: Spectral LDFC experiments with dynamical wavefront disturbances.

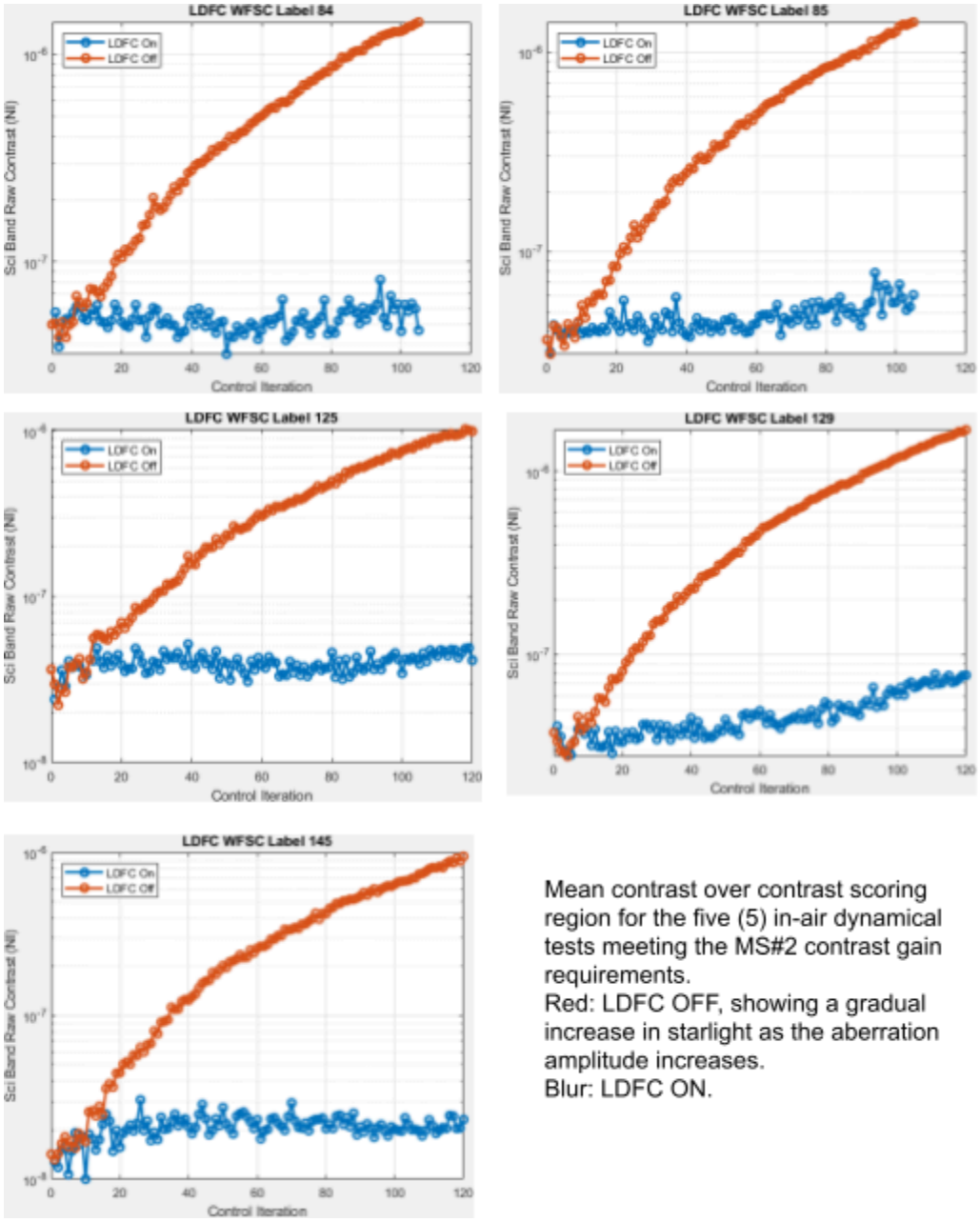


Mean contrast over contrast scoring region for the five (5) in-air dynamical tests meeting the MS#2 contrast gain requirements.
Red: LDFC OFF, showing a gradual increase in starlight as the aberration amplitude increases.
Blur: LDFC ON.

Dynamical tests (Table 2) were conducted in air, prior to the experiment moving in vacuum. Consequently, the contrast level was limited to a few x1e-8 by air instability. Nine (9) dynamical tests were performed, out of which five (5) reached MS#2 requirements, as listed in Table 2. The four remaining tests failed to reach the 10x contrast gain (7.4x, 7.4x, 7.8x and 9.4x for labels #84, #131, #138, #148 respectively). The figure shows contrast evolution with LDFC ON and OFF are shown for each of the 5 tests in the table. All dynamical tests had a loop gain of 0.9 and used a regularized (ridge regression) controller free of leak. The disturbance was a single eigenmode of growing amplitude.

# Conclusion

## Summary of Results

This report presents a successful completion of the Milestone 2 of our Strategic Astrophysics Technology program on Linear Wavefront Control. Milestone 2 focused on demonstrating Spectral Linear Dark Field Control below 1E-7 raw contrast levels and required correcting for injected disturbances by a factor of 10 or greater.

We successfully demonstrated the ability to use spectral LDFC to correct injected disturbances which improved the contrast relative to the open loop case by a ratio of approximately 12 to 170 for static disturbances in vacuum. This was done with for a variety of science band scoring region areas from approximately 10 to 72 square $\lambda_{sci}$/D. Nine (9) tests were performed with dynamic disturbances in air, achieving contrast gains ranging from 7.4x to 18.09x, with five (5) out of nine (9) tests meeting the MS#2 requirements. For each experiment in Table 1 and 2, Spectral LDFC maintains the average dark hole contrast for over 100 control iterations.

We note that we only perturbed the WF with sine modes, and did not include cosine modes. Our control space dimensionality was reduced by 2x due to this choice of subspace. When considering a single spatial frequency corresponding to a speckle position in the focal plane, the wavefront state can be represented by a complex number (2-dimension). Our choice of sine-only modes restricts both sensing and correction to a 1-D axis instead of the full 2-D complex plane. We could demonstrate deep suppression of WF errors because the WF disturbances we injected were by design within our sensing and control subspace. While this self-consistent test is a valid functional demonstration of LDFC, the injected disturbances were not a realistic representation of on-orbit wavefront errors which would span the full (sines+cosines) modal space. A relevant analogy would be the demonstration of a pointing control loop along a single axis (tip) instead of tip+tilt.

Both Spatial and Spectral LDFC provide promising paths forward to maintain dark holes without the need for DM probing and can run faster than traditional PWP and EFC since the bright field has significantly more flux than the dark zone region.

## Lessons Learned and Drawbacks

One of the important lessons learned from this experiment is the importance of tuning the leaks to stabilize the control. Modal control gives us a more precise way to understand the exact behavior of the LDFC WFSC loop. Prior to modal control, we used a Ridge Regression (regularized pseudo-inverse) approach which had a single tuning parameter but lacked the insight into how each mode evolves over time. Another important lesson we learned is the

importance of simulation to develop the software framework to free up the testbed from having to be used to test the software for implementing the spectral LDFC algorithm.

## Changes between Milestone Whitepaper and Final Report

The Milestone Whitepaper (MSWP) called for tests to include "*Single spatial frequency (speckle in focal plane)*" and "random phase screen following power law" wavefront disturbance (section *Injected Disturbances*). Our tests only included sine waves and linear combination of these sine waves instead of arbitrary (sine + cosine) speckles, and did not include phase screen following a power law. This choice was motivated by experimental convenience, keeping the dimensionality (number of modes) low to speed up testing, and by prioritization of contrast performance.

## Future work

Future work will focus on practical aspects of using spectral LDFC for DH maintenance. We plan to show that spectral LDFC can be used to control for the natural drift of a coronagraph testbed. Another open question is understanding what kinds of disturbances cannot be corrected with spectral LDFC. For example, a calibration based on sine waves will mostly not be able to correct for speckles created by a cosine. Therefore we may need to add extra or different kinds of vectors to our basis to enlarge the set of disturbances we can correct for. Especially relevant to answering the question of the need to point a telescope to a bright reference star is the ability to execute spectral LDFC in the low photon flux regime.

Milestone 3 will focus on PSF post-processing and seeks to demonstrate that the spatial or spectral BF can be used to estimate the dark field component, such that the resulting estimate can then be numerically subtracted from the measured dark field. The stated goal will be to "Demonstrate a 10x gain in contrast by post-processing using LDFC telemetry, reaching a post-processed contrast level below 1E-8."

Future activities in active control and PSF reconstruction should explore the full range of modal disturbances (sines + cosines) to validate performance in realistic on-orbit conditions.

# References


- Traub, W. A. and Oppenheimer, B. R., "Direct imaging of exoplanets," in [Exoplanets ], Seager, S., ed., 111–156, University of Arizona Press, 1st ed. (2010).
- Crill, B., "Progress in technology for exoplanet missions: An appendix to the NASA exoplanet exploration program technology plan," (2022). Accessed: 2023-08-3
- Give'on, A., Kern, B. D., and Shaklan, S., "Pair-wise, deformable mirror, image plane-based diversity electric field estimation for high contrast coronagraphy," in [Techniques and

Instrumentation for Detection of Exoplanets V], Shaklan, S., ed., 8151, 815110, International Society for Optics and Photonics, SPIE (2011).
- Give'on, A., Kern, B., Shaklan, S., Moody, D. C., and Pueyo, L., "Broadband wavefront correction algorithm for high-contrast imaging systems," in [Astronomical Adaptive Optics Systems and Applications III], Tyson, R. K. and Lloyd-Hart, M., eds., 6691, 63 – 73, International Society for Optics and Photonics, SPIE (2007).
- Potier, A., Baudoz, P., Galicher, R., Singh, G., and Boccaletti, A., "Comparing focal plane wavefront control techniques: Numerical simulations and laboratory experiments," Astronomy and Astrophysics 635(A192) (2020).
- Give'on, A., "A unified formalism for high contrast imaging correction algorithms," in [Techniques and Instrumentation for Detection of Exoplanets IV], Shaklan, S. B., ed., 7440, 112 – 117, International Society for Optics and Photonics, SPIE (2009)
- Roman Space Telescope at IPAC, "Roman coronagraph instrument post processing report - os9 spc distribution." https://roman.ipac.caltech.edu/docs/sims/Roman CGI post processing report SPC.pdf (2022). Accessed: 2023-08-10.
- Pogorelyuk, L., Krist, J., Nemati, B., Riggs, A. J. E., Miller, S., Pueyo, L., Kasdin, N. J., and Cahoy, K., "Dark hole maintenance with modal pairwise probing in numerical simulations of Roman coronagraph instrument," Journal of Astronomical Telescopes, Instruments, and Systems 8(1), 019002 (2022).
- Pogorelyuk, L. and Kasdin, N. J., "Dark Hole Maintenance and A Posteriori Intensity Estimation in the Presence of Speckle Drift in a High-contrast Space Coronagraph," ApJ 873, 95 (Mar. 2019).
- Redmond, S. M., Kasdin, N. J., Pogorelyuk, L., Soummer, R., Pueyo, L., Perrin, M. D., Maclay, M., Noss, J., Laginja, I., Will, S. D., and Fowler, J., "Implementation of a dark hole maintenance algorithm for speckle drift in a high contrast space coronagraph," in [Space Telescopes and Instrumentation 2020: Optical, Infrared, and Millimeter Wave ], Lystrup, M., Perrin, M. D., Batalha, N., Siegler, N., and Tong, E. C., eds., 11443, 114432K, International Society for Optics and Photonics, SPIE (2020).
- Miller, K., Guyon, O., and Males, J., "Spatial linear dark field control: stabilizing deep contrast for exoplanet imaging using bright speckles," Journal of Astronomical Telescopes, Instruments, and Systems 3(4), 049002 (2017)
- Currie, T., Pluzhnik, E., Guyon, O., Belikov, R., Miller, K., Bos, S., Males J., Sirbu, D., Bond, C., Frazin, R., Groff, T., Kern B., Lozi J., Mazin, B., Nemati, B., Norris, B., Subedi, H., Will, S., "Laboratory Demonstration of Spatial Linear Dark Field Control for Imaging Extrasolar Planets in Reflected Light," Publications of the Astronomical Society of the Pacific, 132:104502, (2020).
- Ahn, K., Guyon, O., Lozi, J., Vievard, S., Deo, V., Skaf, N., Bragg, J., Haffert, S. Y., Males, J. R., and Currie, T., "Laboratory demonstrations of EFC and spatial LDFC on Subaru/SCExAO," in [Adaptive Optics Systems VIII], Schreiber, L., Schmidt, D., and Vernet, E., eds., 12185, 121852B, International Society for Optics and Photonics, SPIE (2022).
- Ahn, K., Guyon, O., Lozi, J., Vievard, S., Deo, V., Skaf, N., Bragg, J., Haffert, S. Y., Males, J. R., and Currie, T., "Combining efc with spatial ldfc for high-contrast imaging on subaru/scexao," Astronomy & Astrophysics 673 (2022).
- Guyon, O., Miller, K., Males, J., Belikov, R., and Kern, B., "Spectral linear dark field control: Stabilizing deep contrast for exoplanet imaging using out-of-band speckle field," (2017).
- Noyes, M. R., Allan, G. W., Walter, A., Ruane, G., and Riggs, A. E. D., "The decadal survey testbed 2: A technology development facility for future exo-earth observatories," in [Techniques and Instrumentation for Detection of Exoplanets XI ], (2023). NKT Photonics, "SuperK FIANIUM laser." https://www.nktphotonics.com/products/supercontinuum-white-light-lasers/superk-fianium/ (2023). Accessed: 2023-08-12.

- NKT Photonics, “SuperK FIANIUM laser.” https://www.nktphotonics.com/products/supercontinuum-white-light-lasers/superk-fianium/ (2023). Accessed: 2023-08-12
- NKT Photonics, “SuperK VARIA tunable filter.” https://www.nktphotonics.com/products/supercontinuum-white-light-lasers/superk-varia/ (2023). Accessed: 2023-08-08.
- Riggs, A. J. E., Ruane, G., Sidick, E., Coker, C., Kern, B. D., and Shaklan, S. B., “Fast linearized coronagraph optimizer (FALCO) I: a software toolbox for rapid coronagraphic design and wavefront correction,” 10698, 878 – 888, International Society for Optics and Photonics, SPIE (2018).
- Poon, P. K., Ng, W., and Sridharan, V., “Image denoising with singular value decompositon and principal component analysis,” Paper for the course Advanced Linear Systems ECE501b, University of Arizona (2009).
- Ruane, G., Wallace, J. K., Riggs, A., Wenger, T., Bagheri, M., Jewell, J., Raouf, N., Allan, G., Prada, C. M., Noyes, M., and Walter, A. B., “Dual purpose lyot coronagraph masks for simultaneous high-contrast imaging and high-resolution wavefront sensing,” in [Techniques and Instrumentation for Detection of Exoplanets XI ],(2023).